CRYSTALLOGRAPHY REPORTS, 2025, Vol. 70, No. 1, pp. 128–134

CRYSTAL GROWTH

ANALYSIS OF CRYSTAL STRUCTURE OF EPITAXIAL NANOHETEROSTRUCTURES WITH MULTIPLE PSEUDOMORPHIC QUANTUM WELLS {$In_xGa_{1-x}As/GaAs$} ON GaAs (100), (110) AND (111)*A* SUBSTRATES

© 2025 E. A. Klimov[a, b], A. N. Klochkov[c], and S. S. Pushkarev[a, *]

[a] National Research Centre "Kurchatov Institute", Moscow, Russia
[b] Orion R&P Association, JSC, Moscow, Russia
[c] National Research Nuclear University "MEPhI", Moscow, Russia
e-mail: s_s_e_r_p@mail.ru

Received August 13, 2024
Revised October 28, 2024
Accepted November 01, 2024

Abstract. The crystal structure of {$In_{0.1}Ga_{0.9}As/GaAs$} × 10 and {$In_{0.2}Ga_{0.8}As/GaAs$} × 10 epitaxial multilayer films on GaAs substrates with different orientations has been studied (100), (110), (111)*A* in order to identify features that may be related to the previously discovered increased efficiency of terahertz radiation generation in films with orientations (110) and (111)*A*. Significant concentrations of twins and package defects were found in films on non-standard GaAs (110) and (111)*A* substrates. The composition and thicknesses of individual layers of heterostructures on GaAs (100) substrates have been refined by analyzing thickness fluctuations on diffraction reflection curves.

DOI: 10.31857/S00234761250118e9

INTRODUCTION

Terahertz (THz) radiation holds great promise for applications in medicine, security systems, environmental monitoring, and broadband data transmission [1–3]. In this regard, research is being conducted to identify the most effective methods for generating and detecting such radiation [4]. Photoconductive antennas – semiconductor devices characterized by high dark resistance and ultrashort photocarrier lifetimes [5] – operate based on the photoconductivity effect under laser pumping and have proven to be practical and efficient THz radiation generators and detectors for use in pulsed THz spectroscopy systems [6]. In such sources, THz radiation generation occurs due to the excitation of fast transient photocurrents in a near-surface electric field [7] or in an external electric field created by the electrodes of the photoconductive antenna [8].

In GaAs and InGaAs semiconductors, the piezoelectric effect arises due to their non-centrosymmetric crystal structure, leading to electric polarization in deformed layers [9]. The combination of multiple layers with different lattice parameters (e.g., $In_xGa_{1-x}As$ and GaAs) within a single epitaxial heterostructure allows the formation of a built-in electric field due to strain effects. The amplitude and direction of this field depend on the crystallographic orientation and the degree of lattice parameter mismatch.

In [10], it was shown that the built-in electric field in strain-engineered multiple quantum wells {InGaAs/GaAs} × 10 influences the efficiency of THz oscillation generation when femtosecond optical laser pulses irradiate the surface of heterostructures, as well as photoconductive antennas fabricated from them. A comparison of THz radiation generated under identical excitation conditions from films with the same composition but grown on substrates with different orientations demonstrated that the most intense THz emission was produced by heterostructures on GaAs(110) substrates. Heterostructures on (111)A substrates were less efficient, while films on standard (100) substrates were the least effective. Among the photoconductive antennas fabricated from these heterostructures, the highest THz generation efficiency was observed in antennas based on films with (110) and (100) orientations.

This study investigates the crystal structure of these epitaxial multilayer films to identify features that may be associated with enhanced THz generation efficiency.

SAMPLES AND RESEARCH METHODS

Nanostructures with pseudomorphically strained multiple quantum wells {$In_xGa_{1-x}As/GaAs$} were synthesized using molecular beam epitaxy (**MBE**). The investigated samples were grown in an MBE CNA-24 system on semi-insulating GaAs substrates

with crystallographic surface orientations (110), (111)A, and (100). Before each growth process, the substrates underwent pre-growth preparation in an As_4 flux at 620°C in the growth chamber. Following this, an undoped 200 nm GaAs buffer layer and a 10-period superlattice $\{In_xGa_{1-x}As/GaAs\}$ with a total thickness of 1100 nm and an indium molar fraction of $x = 0.1$ and 0.2 were grown. (Here, the term "superlattice" is used in a broad sense as a periodic sequence of semiconductor layers that are not necessarily thin and do not necessarily imply the coupling of adjacent quantum wells into a unified band spectrum [11]; a more precise but cumbersome description would be "heterostructures with multiple quantum wells"). The thickness of the InGaAs layers was chosen not to exceed the critical thickness for lattice-mismatched layers of the given composition, ensuring that elastic strain in the layer does not relax, keeping the layer pseudomorphic. InGaAs layers were grown at a lower temperature than GaAs layers. To reduce the interfacial broadening effect of the InGaAs/GaAs heterojunction due to In segregation, a 1 nm GaAs cap layer was grown immediately after the InGaAs layer at a reduced temperature, followed by a growth stop and an increase in substrate temperature to the optimal value for GaAs. The growth temperature T_g was measured and controlled using a thermocouple mounted in the sample holder, while the partial pressures P_{As4}, P_{Ga} and P_{In} were monitored using an Alpert–Bayard gauge in the growth zone. Superlattices on (111)A substrates were grown under two different conditions: with high-temperature barriers and low-temperature wells at a flux ratio of $\gamma = P_{As4}/(P_{Ga} + P_{In})$ ~38 (samples 104, 102) and with an intermediate uniform growth temperature for the entire superlattice at γ ~15 (samples 107, 108). The sample design is shown in Fig. 1, and the growth parameters are listed in Table 1.

It is known that the optimal γ values for homoepitaxial growth on GaAs(100), (110), and (111)*A* substrates differ, with GaAs(111)*A* requiring a lower value [12]. Therefore, heterostructures analogous to samples 104(111)*A* and 102(111)*A* were grown under reduced As_4 pressure, yielding samples 107(111)*A* and 108(111)*A*, respectively.

X-ray diffraction (XRD) reflection curves were measured using an Ultima IV (Rigaku) diffractometer with CuK_α (30 kV, 30 mA, $\lambda = 1.54056$ Å), a Ge(220)×2 crystal monochromator, a parallel beam, a vertical slit DHL 2 mm, horizontal slits DS–RS/SS 0.2–0.5/0.5 mm, a step size of 0.002°, and a counting time of 5 s.

Surface morphology was analyzed by atomic force microscopy (**AFM**) using an NT-MDT Ntegra Maximus microscope in contact mode, with a scanning area of 30 × 30 μm.

The heterostructures were investigated using transmission electron microscopy (**TEM**), energy-dispersive X-ray spectroscopy (**EDX**), and X-ray photoelectron spectroscopy (**XPS**). Cross-sections of the heterostructures for TEM studies (~100 nm thick) were prepared using a focused Ga^+ ion beam. TEM and EDX analyses were performed using a JEM-2100 transmission scanning electron microscope at an accelerating voltage of 200 kV. XPS studies were conducted using a PHI 5000 VersaProbe II X-ray photoelectron spectrometer with monochromatic AlK_α radiation, employing depth profiling via focused Ar^+ ion sputtering at 2 keV. Atomic concentrations were determined using the relative elemental sensitivity factor method based on the measured integral intensities of the Ga3*p*, As3*d*, In3*d*5 lines.

ATOMIC FORCE MICROSCOPY

The surface morphology of the studied samples was described in detail in [13, 14]. The identified surface relief characteristics and measured root-mean-square roughness values, which are highly useful for a more comprehensive study of the crystalline structure of the samples, are summarized in Table 2.

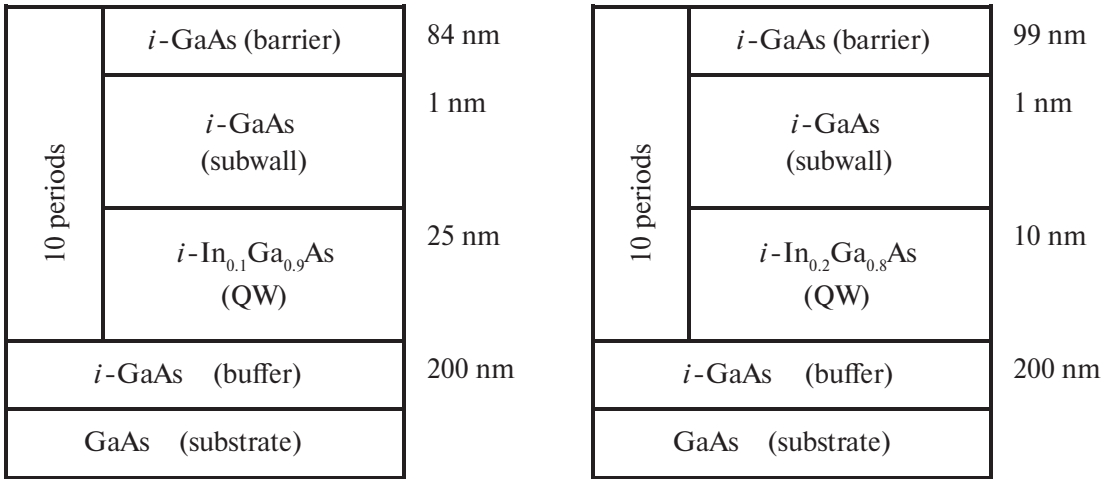

Fig. 1. Design of superlattice nanoheterostructures. QW – quantum well.

Table 1. Parameters of epitaxial growth of heterostructures

Sample	x	Substrate orientation	T_g, °C		Growth rate, Å/min	γ
			Buffer and barrier	QW		
105	0.1	(100)	590	480	120	33
103		(110)	480	430	90	38
104		(111)*A*	480	430	90	39
108			460	460	120	15
106	0.2	(100)	590	480	120	37
102		(110)	480	430	90	38
102		(111)*A*	480	430	90	38
107			460	460	120	15

Note: x is the mole fraction of indium in the quantum well (QW), T_g is the growth temperature, γ is the ratio of the As_4 pressure to the sum of the In and Ga pressures.

These data complement the conclusions drawn from TEM measurements. Surface roughness is an easily measurable quantitative parameter that allows for the assessment of the crystalline quality of the grown films without the need for more resource-intensive TEM measurements. Based on surface roughness, it can be concluded that the growth conditions of samples 107 and 108 were suboptimal: these films were less smooth than all others (except for sample 104). The root-mean-square surface roughness of sample 107 (111)*A*,

Table 2. Surface morphology according to AFM images and features of the crystal structure of the films under study according to TEM images

	$x = 0.10$	$x = 0.20$
Substrate orientation (100)	Surface texture: cross-hatch (R_q = 1.5 nm) In film thickness: no defects ($D < 0.6$ μm^{-2}). Heteroboundaries: clear, flat *sample 105* (100)	Surface texture: cross-hatch (R_q = 1.9 nm) In the thickness of the film: twins (α = 55°–56°, $D \approx 2$ μm^{-2}), dislocations ($D \approx 1$ μm^{-2}) Heteroboundaries: clear, flat *sample 106* (100)
Substrate orientation (110)	Surface relief: chaotic, uniformly distributed tubercles and depressions 0.4 × 0.5 μm (R_q = 13.7 nm) In the thickness of the film: numerous twins (α = 0° or 71°, $D \approx 20$ μm^{-2}), individual dislocations ($D \sim 0.6$ μm^{-2}). Heteroboundaries: fuzzy, curved *sample 103* (110)	Surface topography: parallel straight ridges (R_q = 3.4 nm) In the thickness of the film: twins (α = 35°, $D \approx 3$ μm^{-2}), individual dislocations ($D \sim 0.6$ μm^{-2}). Heteroboundaries: clear, flat *sample 102* (110)
Substrate orientation (111)*A*	Surface relief: chaotic, individual high islands 0.5 × 1.0 μm (R_q = 25.8 nm) In the thickness of the film: twins (α = 0° or 64°, $D \approx 9$ μm^{-2}), individual stacking faults ($D \sim 0.6$ μm^{-2}). Heteroboundaries: fuzzy *sample 104* (111)A	Surface topography: anisotropic, oriented elongated grains 0.2 × 0.4 μm (R_q = 8.2 nm) In the thickness of the film: numerous dislocations ($D \approx 9$ μm^{-2}), individual twins ($D \sim 0.6$ μm^{-2}) Heteroboundaries: fuzzy, curved *sample 102* (111)A

Note: R_q is the root mean square roughness over a field of 30 × 30 μm, α is the angle between the twins and the growth plane, D is the density of defects, i.e. number of defects crossing 1 μm^2 cross-section area of the sample, heterointerfaces – boundaries between the GaAs and $In_xGa_{1-x}As$ layers.

measured over a 30 × 30 μm area, is R_q = 20.8 nm, while for sample 108 (111)*A*, it is 22.9 nm. Therefore, these samples were not investigated using TEM.

TRANSMISSION ELECTRON MICROSCOPY

Electron diffraction and contrast in TEM images indicate that the studied films can be conditionally considered monocrystalline, though in some cases they exhibit twinning, dislocations, and wedge-shaped defects. A clear difference in defect density is observed among heterostructures with identical nominal compositions grown on substrates of different orientations.

First, we examine heterostructures with a low indium molar fraction of $x = 0.1$. In heterostructure 105 on a GaAs(100) substrate, no defects were detected (Fig. 2a). The layer boundaries appear sharp and planar, and the measured layer thicknesses correspond to the nominal values.

Heterostructure 103 on a GaAs(110) substrate exhibits polysynthetic twinning. Individual dislocations are also present in the sample, though they are not visible in the provided images. Figure 2b shows twins oriented either along the substrate plane or at an angle of 71° to it, with widths of approximately 10–30 nm. The layer boundaries are poorly distinguishable. It is possible that the relaxation of elastic stresses in the sample occurs primarily through twin formation. Heterostructure 104 on a GaAs(111)*A* substrate contains twins and stacking faults (Figs. 2c, 3). The layer boundaries are also poorly distinguishable.

Microanalysis of the indium-containing $In_xGa_{1-x}As$ ayers in sample 105 using EDS revealed an indium mole fraction x of approximately 17 at.%, while XPS microanalysis with depth profiling using a cluster ion beam (analyzing only the top three $In_xGa_{1-x}As$ layers) indicated an indium mole fraction of approximately 7 at.%. Similar measurements for other samples are challenging due to the defectiveness of the heterostructures on (110) and (111) substrates, where the In-containing layers are poorly distinguishable.

Fig. 4 presents TEM images of dislocations in heterostructures with a high indium molar fraction of $x = 0.2$. It can be seen that heterostructure 106 on a GaAs(100) substrate contains twins and individual dislocations (Fig. 4a). Heterostructure 102 on a GaAs(110) substrate also contains twins and individual dislocations (Fig. 4b). The layer boundaries are sharp and planar, and the measured layer thicknesses correspond to the nominal values. Heterostructure 102 on a GaAs(111)*A* substrate exhibits numerous dislocations (Fig. 4c) and some twins. The layer boundaries are poorly distinguishable.

The main features of the crystalline structure of the samples, as observed using TEM, are summarized in Table 2. The results suggest that heterostructures with more strained InGaAs layers (i.e., with a higher indium molar fraction) formed with more defects than those with a lower indium molar fraction. Additionally, films on (110) and (111)*A* substrates exhibit a higher defect density than those on (100) substrates.

HIGH-RESOLUTION X-RAY DIFFRACTOMETRY

First, let us consider the superlattices on GaAs(100) substrates. The XRD patterns of samples 105 ($x = 0.1$) and 106 ($x = 0.1$) in the 2θ/ω geometry exhibit distinct satellite peaks, indicating the presence of a superlattice, along with a broad peak corresponding to strained $In_xGa_{1-x}As$ (Fig. 5). Using the Rigaku GlobalFit software, a model XRD pattern for the $\{In_xGa_{1-x}As/GaAs\} \times 10$ superlattice was calculated and then fitted to the experimental XRD data by adjusting the model layer thicknesses of $In_xGa_{1-x}As$ and GaAs, as well as the composition parameter x. The model assumed the absence of partial relaxation of the strained crystal lattice. The model parameters that yielded a good fit to the experimental data are presented in Table 3, showing that they closely match the nominal values.

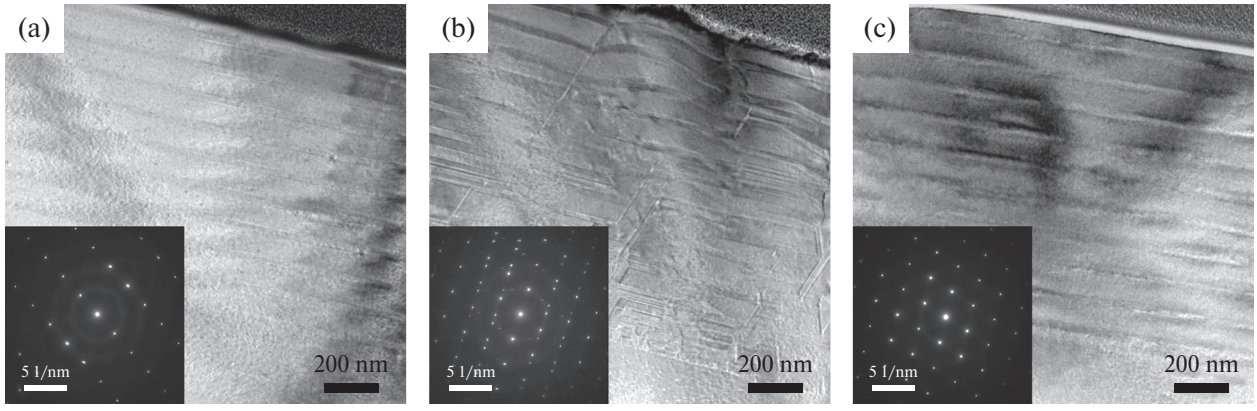

Fig. 2. Bright-field TEM images of samples: a – 105 (100), b – 103 (110), 104 (111)*A*. The insets show the corresponding electron diffraction patterns.

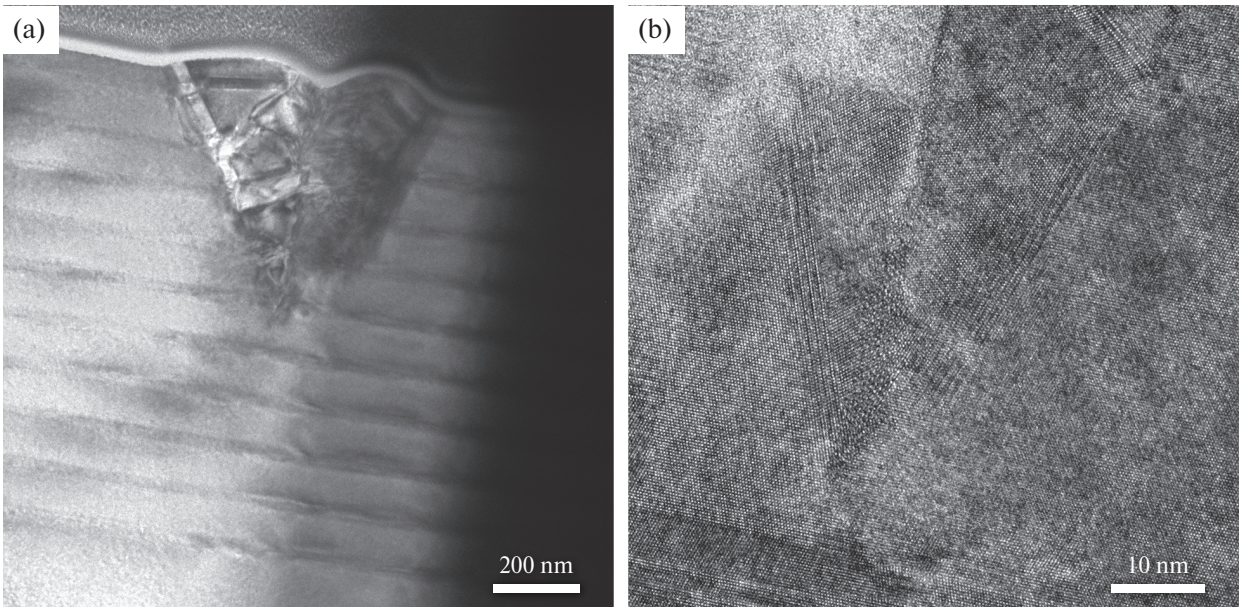

Fig. 3. Defects in sample 104 (111)*A*: a – a defect formed in the middle of the film thickness and growing onto the surface, bright-field TEM image; b – twinning and packing defects, high-resolution image.

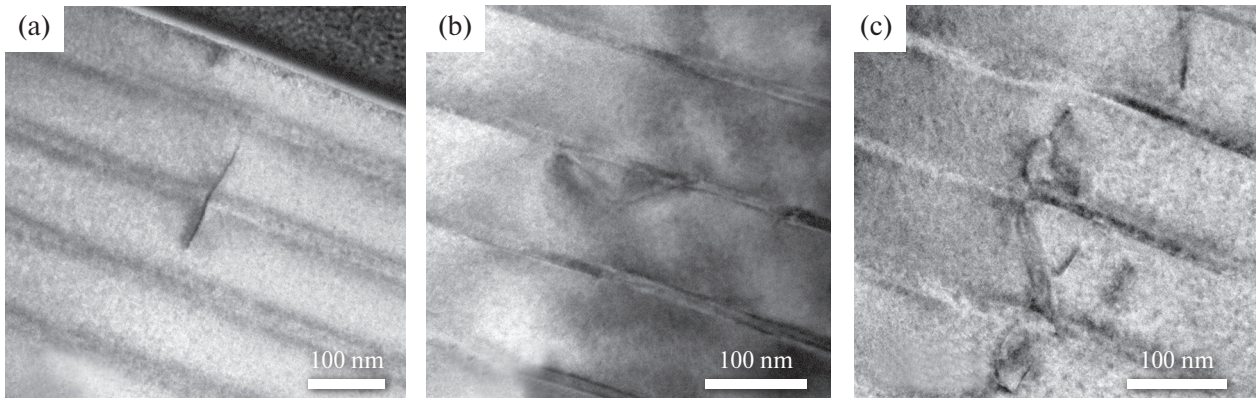

Fig. 4. Bright-field TEM images of dislocations in the samples: a – 106 (100), b – 102 (110), c – 102 (111)*A*.

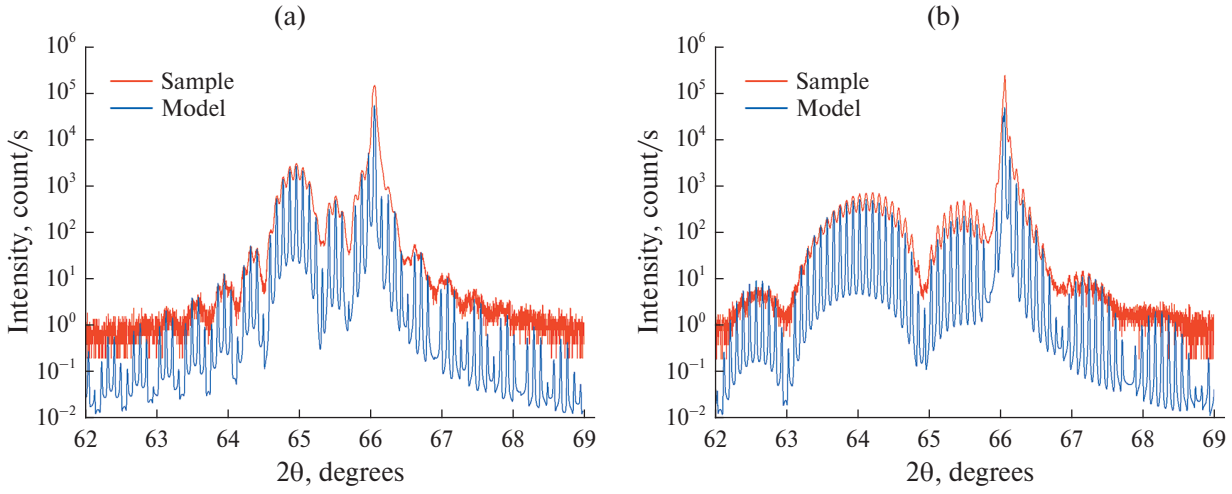

Fig. 5. XRD curves 004 of samples 105 (a) and 106 (b) on GaAs(100) substrates.

Table 3. Thicknesses and composition of superlattice layers on standard GaAs(100) substrates, determined using X-ray diffractometry

Layer	$\{In_{0.1}Ga_{0.9}As/GaAs\}\times 10$			$\{In_{0.2}Ga_{0.8}As/GaAs\}\times 10$		
	Thickness, nm	Mole fraction of indium x	Deformation ε	Thickness, nm	Mole fraction of indium x	Deformation ε
GaAs	87.6	0	0	103.4	0	0
$In_xGa_{1-x}As$	26.4	0.114	0.0082	10.9	0.212	0.0152

This approach allows for a fairly accurate determination of the composition x of the $In_xGa_{1-x}As$ layer, as well as the superlattice period: d = 114.0 nm for $\{In_{0.1}Ga_{0.9}As/GaAs\} \times 10$ and d = 114.3 nm for $\{In_{0.2}Ga_{0.8}As/GaAs\} \times 10$. However, the individual thicknesses of the GaAs and $In_xGa_{1-x}As$ layers are determined with lower accuracy, since it is the superlattice period that primarily defines the angular positions of the satellite peaks.

Additionally, asymmetric XRD patterns (422 reflections) were measured, where the incident X-ray angle differs from the reflection angle. These measurements were performed in two geometries: one with a small incidence angle (6.62°) and a large diffraction exit angle (77.15°), and another with a large incidence angle and a small diffraction exit angle (Fig. 6). The difference between the XRD patterns in these two cases arises from the varying effective thickness of the diffracting layer: at a grazing incidence, the X-ray beam interacts with a significantly greater number of reflecting planes than at a steep incidence, leading to an overall increase in signal intensity and the appearance of more features in the XRD pattern.

Regarding the superlattices on GaAs(110) substrates, little can be said. A comparison of the symmetric 220 and 440 reflections from the GaAs substrate showed that the 220 reflection produces a slightly more pronounced shoulder on the left side of the dominant peak and a higher overall signal intensity than the 440 reflection. No interference oscillations were observed.

For superlattices on GaAs(111)*A* substrates, weak oscillations were detected in the XRD patterns of samples 102(111)*A* and 104(111)*A* (Fig. 7), indicating sharper and more planar heterointerfaces in these samples compared to samples 107(111)*A* and 108(111)*A*.

CONCLUSION

It has been shown that epitaxial growth on non-standard GaAs(110) and GaAs(111)*A* substrates is accompanied by an increased density of twin defects and stacking faults. Films with an indium mole fraction of x = 0.1 contain significantly more twins than those with x = 0.2 (over 20 and 3 μm^{-2}, respectively). The surface morphology of the films retains anisotropic features (elongated, uniformly oriented islands) at moderate defect concentrations but becomes isotropic

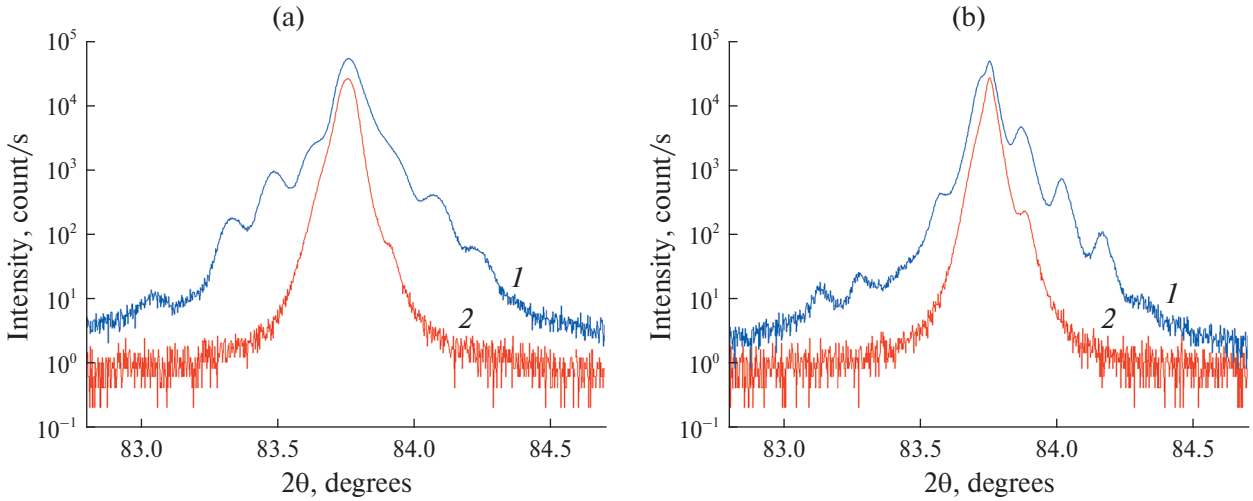

Fig. 6. Asymmetric XRD curves 422 for samples 105 (a) and 106 (b) on GaAs(100) substrates at small angles of incidence (1) and small angles of reflection (2).

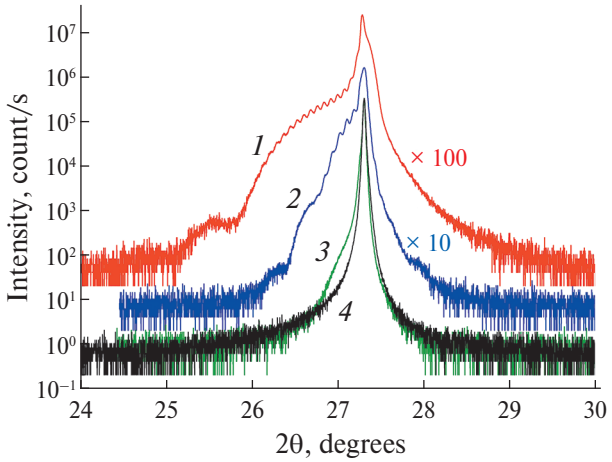

Fig. 7. XRD curves 111 of samples 102 (1), 104 (2), 107 (3), 108 (4) on GaAs(111)*A* substrates, for better visualization of the DRC are spaced vertically.

(round islands) at higher defect concentrations. Dislocations and twins also appear at low densities (1 and 2 μm^{-2}, respectively) in films grown on standard GaAs(100) substrates when the heterostructure includes pseudomorphically strained layers with a sufficiently high indium mole fraction of $x = 0.2$.

Based on TEM images, one might conclude that the highest-quality crystalline films grow on GaAs(100) substrates, lower-quality films grow on GaAs(110), and the least perfect films grow on GaAs(111)*A*. However, this is contradicted by XRD thickness oscillations, which were observed in films grown on GaAs(111)*A* substrates but not on GaAs(110), suggesting that the latter are more defective.

By analyzing thickness oscillations in XRD 100 scans recorded in the 2θ/ω mode for the highest-quality crystalline samples on GaAs(100) substrates, the design (composition and layer thicknesses) of the samples was refined. The actual parameters were found to be very close to the nominal ones: the barrier thickness was 3 % greater than the nominal value, the quantum well thickness was 6–9 % greater, and the indium mole fraction in the quantum well was 6–14 % higher. Compared to XRD thickness oscillation analysis, EDX and XPS methods provided only rough, order-of-magnitude estimates of the composition of nanometer-thick layers.

FUNDING

The study was supported by the Russian Science Foundation grant No. 22-19-00656 (https://rscf.ru/en/project/22-19-00656/), epitaxial growth was performed with the financial support of NRC "Kurchatov Institute". TEM measurements were carried out at the Center for Collective Use "Materials Science and Metallurgy" of NUST MISIS.

CONFLICT OF INTERESTS

The authors declare that they have no conflict of interest.

REFERENCES

1. *Naftaly M., Vieweg N., Deninger A.* // Sensors. 2019. V. 19. P. 4203. https://doi.org/ 10.3390/s19194203
2. *Consolino L., Bartalini S., De Natale P.* // J. Infrared Millim. Terahertz Waves. 2017. V. 38. P. 1289.
3. *Hafez H.A., Chai X., Ibrahim A. et al.* // J. Opt. 2016. V. 18. P. 093004. https://doi.org/10.1088/2040-8978/18/9/093004
4. *Dhillon S.S., Vitiello M.S., Linfield E.H. et al.* // J. Phys. D. 2017. V. 50. P. 043001. https://doi.org/10.1088/1361-6463/50/4/043001
5. *Krotkus A.* // J. Phys. D. 2010. V. 43. P. 273001. https://doi.org/10.1088/0022-3727/43/27/273001
6. *Burford N.M., El-Shenawee M.O.* // Opt. Eng. 2017. V. 56. P. 010901. https://doi.org/10.1117/1.OE.56.1.010901
7. *Apostolopoulos V., Barnes M.E.* // J. Phys. D. 2014. V. 47. P. 374002. https://doi.org/10.1088/0022-3727/47/37/374002
8. *Castro-Camus E., Alfaro M.* // Photon. Res. 2016. V. 4. P. A36. https://doi.org/10.1364/PRJ.4.000A36
9. *Ilg M., Ploog K.H., Trampert A.* // Phys. Rev. B. 1994. V. 50. No. 23. P. 17111. https://doi.org/10.1103/PhysRevB.50.17111
10. *Klimov E. A., Klochkov A. N., Solyankin P. M. et al.* // Bulletin of the Lebedev Physics Institute. 2024. Vol. 51. Suppl. 4. P. S316–S325. https://doi.org/10.3103/S1068335624601286
11. *Shik A.Ya.* *Superlattice* // Great Russian Encyclopedia: scientific and educational portal. https://bigenc.ru/c/sverkhreshiotka-a2f3e5/?v=5490666
12. *Yerino Christopher D., Liang Baolai, Huffaker Diana L. et al.* // J. Vac. Sci. Technol. B. 2017. V. 35. P. 010801. https://doi.org/10.1116/1.4972049
13. *Klimov E.A., Pushkarev S.S., Klochkov A.N. et al.* // Russian Microelectronics. 2023. V. 52. No. 3. P. 129–134. https://doi.org/10.1134/S106373972370035X
14. *Klimov E.A., Pushkarev S.S., Klochkov A.N.* // Nano- and microsystem technology. 2022. V. 24. No. 6. P. 283. https://doi.org/10.17587/nmst.24.283-287